Fig. 9.   7.5-GHz MIC detector time-domain simulation.

provided an explanation as to why the 34-GHz MMIC detector reported in [5] was 22 dB less sensitive than the 7.5-GHz MIC. This also agrees with the theory of [3] since the MMIC has a lower loop gain; hence, less regeneration is present in the circuit, giving poorer sensitivity.

Therefore, to obtain a sensitive super regenerative detector, the quench voltage should be adjusted at a point where the rate of change of loop gain (or negative resistance) rises most rapidly at oscillator start up. This observation may also have design implications, as circuits could be designed specifically to possess a sharp rise in loop gain. Also, from the simulation results, it could be determined what type of quench waveform would be required for optimum sensitivity.

F. Time-Domain Analysis of RF Envelope

To determine the behavior of the super regenerative detector circuit under actual quenching conditions, a time-domain simulation using HP-MDS was carried out. To be able to simulate several quench cycles while maintaining the total number of time steps below CPU and memory restrictions, a sinusoidal quench frequency of 25 MHz was used instead of the measured 1-MHz range. Two simulations were carried out: one with no applied RF signal and another with a -40-dBm 8-GHz signal applied to the output port. The simulation result of Fig. 9 show that the oscillations are slightly advanced in the presence of an external RF signal, correlating with the findings of [1]–[3]. Another observation is that the oscillations show the effect of the dynamic quenching, as illustrated in Fig. 7. Fig. 9 shows the oscillations beginning to commence at a quench voltage of -0.3 V and not ceasing fully until the quench voltage has reached 0.6 V, indicating the oscillations to "run on" slightly when dynamically quenched.

IV. CONCLUSIONS

Results have been reported in this paper for a MIC detector operating at 7.5 GHz and comparisons made with a 34-GHz MMIC detector [5]. The 7.5-GHz detector was measured to detect a -83-dBm (AM, 1 kHz, 100% mod) RF signal for 12-dB SINAD compared to -61 dBm in the 34-GHz case. An optimum quenching frequency was found experimentally, which agreed with the findings of [2] and [3]. A spectrum display showed the detection frequency to be lower than the normal free-running frequency of the oscillator by typically 0.3 GHz. This was caused by the frequency-pushing effect of the quench signal applied to the gate of the active device, which was confirmed by small-signal loop-gain analysis.

Simulation of the loop gain and measured results of the 7.5- and 34-GHz super regenerative detectors has devised a design philosophy. Namely, the requirement for a sensitive detector to have a high rate of increase in loop gain and a high overall maximum loop gain at the point of detection.

REFERENCES

[1] E. H. Armstrong, "Some recent developments of regenerative circuits," *Proc. Inst. Radio Eng.*, vol. 10, pp. 244–260, Aug. 1922.
[2] H. Ataka, "On superregeneration of an ultra-short-wave receiver," *Proc. Inst. Radio Eng.*, vol. 23, pp. 841–884, Aug. 1935.
[3] F. W. Frink, "The basic principles of super-regenerative reception," *Proc. Inst. Radio Eng.*, vol. 26, pp. 76–106, Jan. 1938.
[4] R. Feick and O. Rojas, "Modeling and simulation of the superregenerative receiver," *IEEE Trans. Consumer Electron.*, vol. 43, pp. 92–102, May 1997.
[5] N. B. Buchanan, V. F. Fusco, and J. A. C. Stewart, "A K_a band super regenerative detector," in *Proc. IEEE MTT-S Int. Microwave Symp. Dig.*, Boston, MA, June 2000, pp. 1585–1588.
[6] N. B. Buchanan, R. Davies, and J. A. C. Stewart, "MMIC K_a band oscillator," *Electron. Lett.*, vol. 32, no. 4, pp. 354–355, Feb. 1996.
[7] W. J. Cunningham, *Introduction to Nonlinear Analysis*.   New York: McGraw-Hill, 1958, pp. 301–320.

An Improved Prediction of Series Resistance in Spiral Inductor Modeling With Eddy-Current Effect

Ban-Leong Ooi, Dao-Xian Xu, Pang-Shyan Kooi, and Fu-Jiang Lin

Abstract—Based on Kuhn's earlier study on current crowding, an improved expression incorporating the skin effect for the prediction of series resistance in spiral inductor modeling has been derived. A modified model for the spiral inductor, which accounts for the eddy-current effect, is thus proposed. Relatively good agreements between the measured data and the results generated from the model are obtained.

Index Terms—Deembedding, eddy current, quality factor, series resistance, skin effect, spiral inductor.

I. INTRODUCTION

The eddy current, which has a significant effect on the inductance of a monolithic-microwave integrated-circuit (MMIC) spiral inductor, manifests itself not only as skin effect, but also as a proximity effect. At around 1 GHz, it is demonstrated in [1] that the proximity effect between the turns of a MMIC spiral inductor (normally on the cross section of the inductor where the width of the metallic trace is relatively much larger than the thickness) that are in the same plane can be neglected. For frequency below 2 GHz, the skin effect is relatively small in most instances since the metallic trace thickness is typically less than or equal to the skin depth. For frequency above 2 GHz, the resistance increases as the skin effect becomes more prominent [2]. In general, all these effects should be included in the inductor circuit modeling. However, to date, this major current crowding mechanism is missing in the conventional inductor equivalent-circuit modeling [3]–[7]. The

incorporation of these effects in the spiral inductor modeling is thus the subject of this paper.

In this paper, based on Kuhn and Ibrahim's study on current crowding [2], we incorporate the skin effect and develop approximate formulas for the series resistance in the spiral inductor modeling. As a result of this, a modified model for the MMIC spiral inductor, which accounts for the eddy-current effect, is thus proposed. As compared to the conventional equivalent-circuit modeling, the proposed circuit is more intuitional and accurate.

II. EDDY-CURRENT CALCULATION

As explained in [2] and [8], the basic mechanism for current crowding lies in the current redistribution caused by the B-field variation on the adjacent turn. It is noted in [2] that the B-field can actually adopt a simplified expression given as

$$B(n) \approx \frac{(n-M)B_0}{N-M} = \frac{0.65\mu_0(n-M)I_{\text{ex}}}{P(N-M)} \qquad (1)$$

where n is the index for the turn number, N is the total number of turns, B_0 is the field at the innermost turn (turn number N), M is the turn number where the field falls to zero and reverses direction, μ_0 is the permeability of free space, P is the turn pitch (illustrated in Fig. 1), and I_{ex} is the excitation current. Using this expression together with the attenuation of the current density in [4], i.e.,

$$J = \begin{cases} J_0 e^{(z-T/2)/\delta}, & \frac{T}{2} \ge z \ge 0 \\ J_0 e^{(-z-T/2)/\delta}, & 0 \ge z \ge -\frac{T}{2} \end{cases} \qquad (2)$$

where T is the inductor thickness and applying them into the Faraday's law, the new per unit length surface eddy current for the nth turn becomes

$$\left| I_n^{\text{eddy}} \right| = 2 \int_0^{T/2} \int_0^{W/2} x\omega\sigma B(n) e^{-z/\delta} \, dx dz$$
$$= \frac{\mu_0 |n-M| 0.162\omega\sigma W^2 I_{\text{ex}} \delta \left(1-e^{-T/(2\delta)}\right)}{P(N-M)} \qquad (3)$$

where W is the inductor width, δ refers to the skin depth, and σ and μ are, respectively, the conductivity and permeability of the metallic trace. In the above derivation, we have assumed that the eddy current on the top and bottom surfaces of the metallic trace is equal. In general, these eddy currents are not the same. By Bio–Savart law, we know that there are two types of electric fields being generated when the current begins to oscillate slowly [9]. The first type is due to the changing magnetic field according to Faraday's law and is not dependent on both the substrate and ground plane. The second type of electric field is due to the changes in charges flow through the current continuity equation. This type of field is affected by the dielectric substrate and ground plane. Equation (3) only models the former effect and the latter effect has been brought forward to the substrate effect. This substrate effect will be covered in a future paper.

III. TOTAL SERIES RESISTANCE CALCULATION

With the presence of the eddy current, it will cause the electrical transmission loss through the metallic trace to increase and, thus, the inductor's series equivalent resistance will be affected. To match the result of this current crowding, we assume that the direction of the eddy-current loop on the inner edge of the metallic trace coincides with the initial excitation current, and we shall consider this for the phase difference between them in the next step.

The power dissipated in the nth turn due to the eddy currents is thus given as follows:

$$P_n^{\text{eddy}} = 4\sigma l_n \omega^2 B^2(n) \cdot \int_0^{T/2} \int_0^{W/2} x^2 e^{-2z/\delta} \, dx dz$$
$$= \frac{\sigma l_n \omega^2 B^2(n) W^3 \delta \left(1-e^{-T/\delta}\right)}{12} \qquad (4)$$

where l_n is the length of the nth turn. Here, the difference in length between the outer eddy-current loop and inner loop near each trace corner is neglected.

Since

$$P_n^{\text{ex}} = I_{\text{ex}}^2 R_n^{\text{dc}} = I_{ex\cdot n}^2 \frac{l_n}{\sigma W T} \qquad (5)$$

where R_n^{dc} is the nth-turn dc resistance, the total power becomes

$$P_n = \sum_n \left(P_n^{\text{ex}} + P_n^{\text{eddy}}\right)$$
$$= I_{\text{ex}}^2 \left(\sum_n R_n^{\text{dc}} \left[1 + \frac{0.14W^4 T \left(1-e^{-T/\delta}\right)\mu_0^2(n-M)^2}{\mu^2\delta^3 P^2(N-M)^2}\right]\right) . \qquad (6)$$

The total spiral resistance R_{total}, which is given by the term enclosed by the first bracket of (6), is more accurate than [2, eq. (17)]. This expression is both geometry and frequency dependent. At low frequency, the total resistance in (6) becomes

$$R_{\text{total}} = R_o \left[1 + \frac{\omega^{2/3} \left(0.05W^4 T\sigma^{2/3}\mu_o^2\right)}{\mu^{1/2}P^2} \sum_n \left(\frac{n-M}{N-M}\right)^2\right] \qquad (7)$$

whereas, at high frequency, with the Taylor's expansion, the total resistance becomes

$$R_{\text{total}} = R_o \left[1 + \frac{\omega^2 \left(0.035W^4 T^2\sigma^2\mu_o^2\right)}{P^2} \sum_n \left(\frac{n-M}{N-M}\right)^2\right] . \qquad (8)$$

IV. CIRCUIT-MODEL IMPROVEMENT

Fig. 2 shows the conventional model of a spiral inductor on the GaAs substrate. The inductance and resistance of the metallic trace of the spiral inductor and the underpass are, respectively, represented by the series inductance L_s and the series resistance R_s. C_s refers to the series capacitance and the other components in the circuit are used to model the substrate effect [4].

Our new approach is to represent the eddy currents as electrical components by modifying the conventional circuit model using results from Section III. If we assume that the source of the eddy-current loop is induced by the excitation current, the ratio of R_{eddy} and L_{eddy} will produce a constant degree of phase delay. The field changing in each turn n will surely be more sensitive due to the current in that turn itself than in those adjacent turns or further ones. Thus, regardless of the turn number n, the eddy-current effect on the two-port transmission network of the spiral inductor will provide us a new idea to modify the conventional circuit model to that shown in Fig. 3.

The branch constituted by L_s' and R_s' and in parallel with R_s is taken as circuit elements contributing to the overall eddy-current loss. The voltage over R_s represents the total voltage effect of each induced eddy-current's segment. Compared with the conventional spiral inductor model in Fig. 3, the new model has an added advantage. By
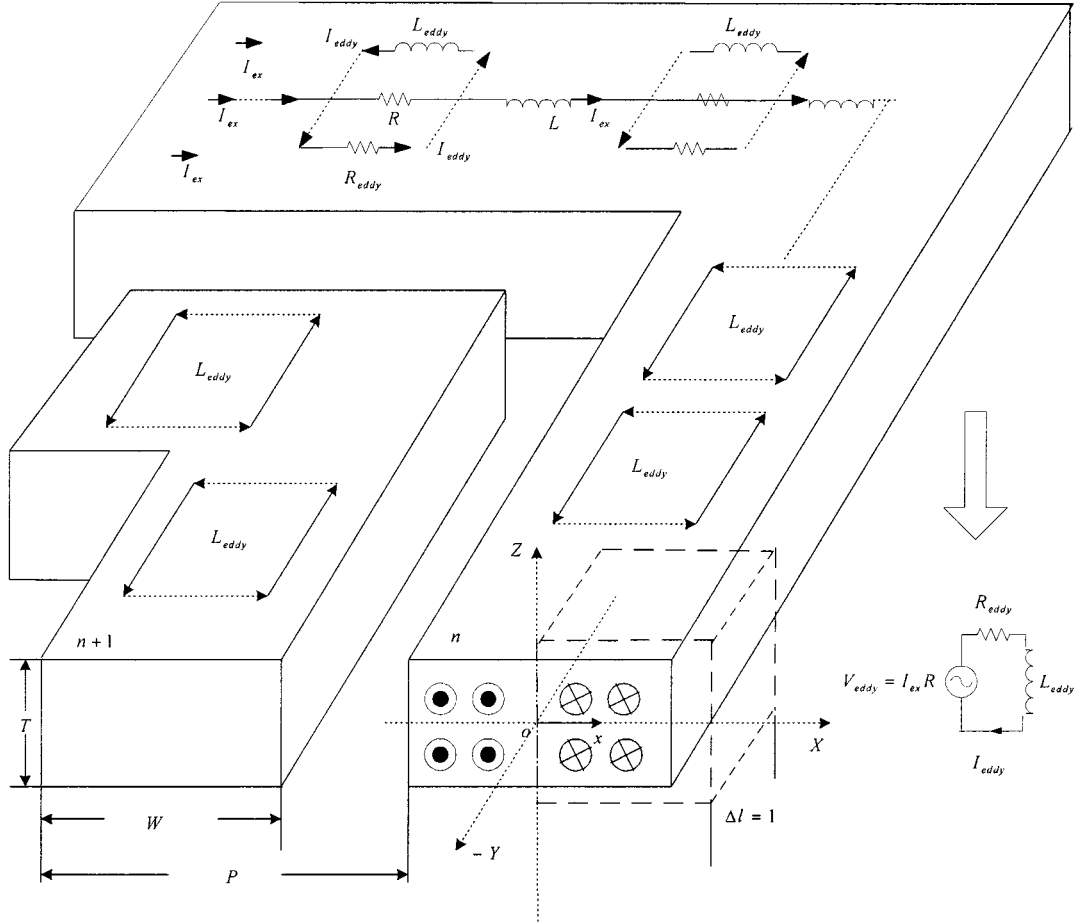
Fig. 1.   Simplified illustration of an eddy-current's effect. The black dot indicates the outgoing current. The cross indicates the incoming current.
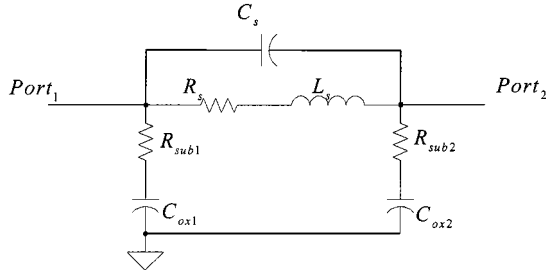

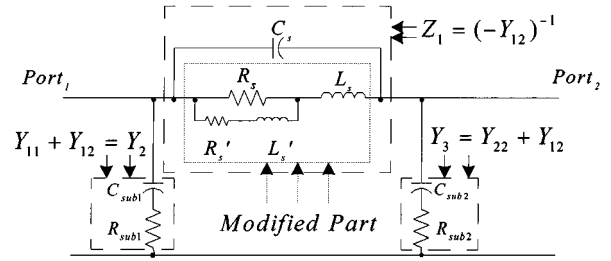Fig. 2.   Conventional circuit model for spiral inductor on the GaAs substrate.

Fig. 3.   Modified circuit model for spiral inductor on the GaAs substrate.

circuit theory

$$\mathrm{Re}\,(Z_{\mathrm{in}}) = R_s - \frac{R_s^2\left(R_s + R_s'\right)}{\left(R_s + R_s'\right)^2 + \omega^2 L_s'^2} \qquad (9)$$

$$\frac{\mathrm{Im}\,(Z_{\mathrm{in}})}{\omega} = L_s + \frac{R_s^2 L_s'}{\left(R_s + R_s'\right)^2 + \omega^2 L_s'^2} \qquad (10)$$

where Z_{in} is the input impedance of the inductor, (9) and (10) provide a frequency varying effect for both the resistance and inductance. This overcomes the limitation of the conventional circuit model in that it can only offer constant value for both the resistance and inductance.
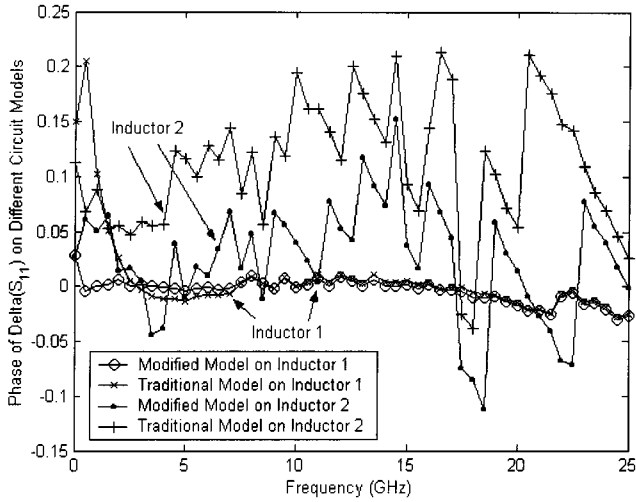
V. EXPERIMENTAL RESULTS

To confirm that the physical model can indeed predict the overall inductor behavior, the one-port S-parameters for two sets of square gold-traced inductors fabricated on the GaAs substrate are measured and mod-

eled. The layout parameters of inductor 1 include 1.75 turns, 10-μm width, 15-μm pitch, and 100-μm outer dimension. It has a metal thickness of 1.5 μm. As for inductor 2, the dimensions include five turns, 26-μm width, 30-μm pitch, and 105-μm outer dimension. It has a metal thickness of 1.8 μm. The one-port S-parameters of the inductors are measured by using the vector network analyzer and coplanar probes.

Figs. 4 and 5 provide the simulation results on the inductors. For clarity, the differences in the simulated S_{11} values with respect to the measured S_{11}, denoted as $\mathrm{Delta}(S_{11})$, for both the inductors are plotted. As noted from these figures, the new model provides more accurate results than the conventional model. It has the lowest error in the lower frequency range, typically below 10 GHz. This trend has also been observed for other inductors with different turn numbers, spacing, and width, which we have fabricated using several external foundries. For brevity, these results are not presented in this paper.

Fig. 3 also shows a general π-model of the equivalent circuit for the spiral inductor. We use the IC-CAP for components extraction and
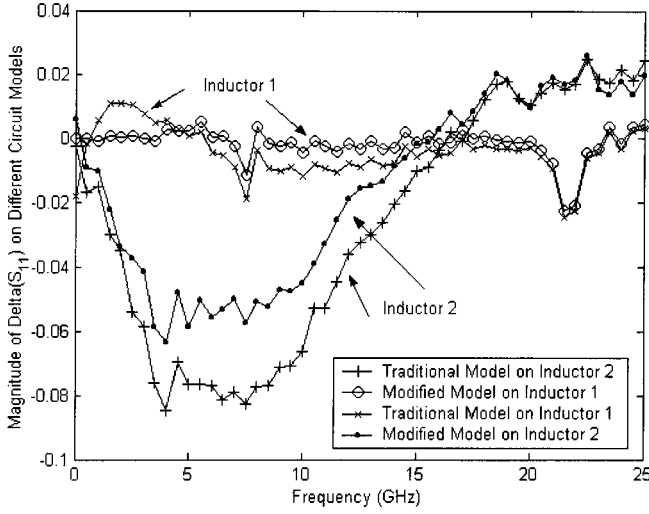
Fig. 4.   Magnitude of S-parameter simulation results on different circuit models.

Fig. 6.   Real part of inductor input impedance after deembedding.

Fig. 5.   Phase of S-parameter simulation results on different circuit models.
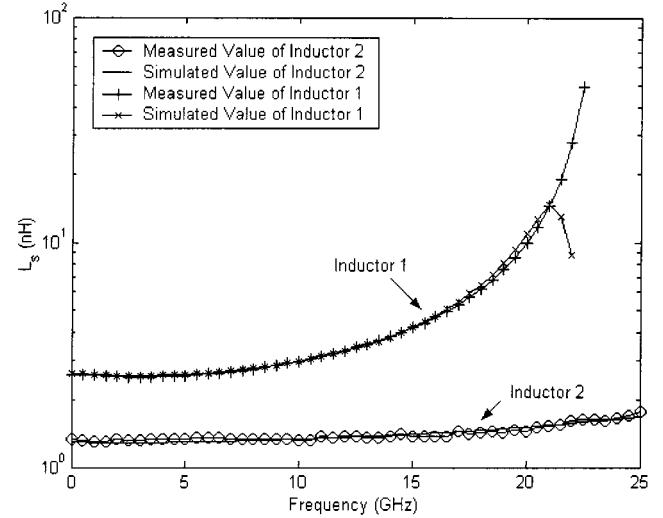
Fig. 7.   Simulation results of imaginary part of Z_1 divided by angular frequency ($\sim L_s$).

optimization. The deembedded Y-parameters in terms of the measured Y-parameters data is given as

$$Y'_{11} = Y_{11} - j\omega C_s - \left(R_{\mathrm{sub1}} + (j\omega C_{\mathrm{ox1}})^{-1}\right)^{-1} \tag{11}$$

$$Y'_{12} = Y_{12} + j\omega C_s \tag{12}$$

$$Y'_{21} = Y_{21} + j\omega C_s \tag{13}$$

$$Y'_{22} = Y_{22} - j\omega C_s - \left(R_{\mathrm{sub2}} + (j\omega C_{\mathrm{ox2}})^{-1}\right)^{-1}. \tag{14}$$

where the superscript $'$ denotes the modified data after deembedding. Fig. 6 illustrates the real part of $-(Y_{12})^{-1}$ for both the inductors. As shown in this figure, the increasing trend of both inductors agrees well with our prediction in Section III. The predicted curve (1) refers to (7), whereas the predicted curve (2) refers to (8).

Fig. 7 gives the simulated results of the imaginary part of $-(Y_{12})^{-1}$. Good agreements between the simulated and measured data for both inductors have been obtained. As shown in Fig. 7, our proposed model fits very well between the frequency ranges of 1–20 GHz. The high-frequency discrepancy, namely, at above 20 GHz for inductor 1, is caused by the fact that the second type of field variation has not been included in our model.
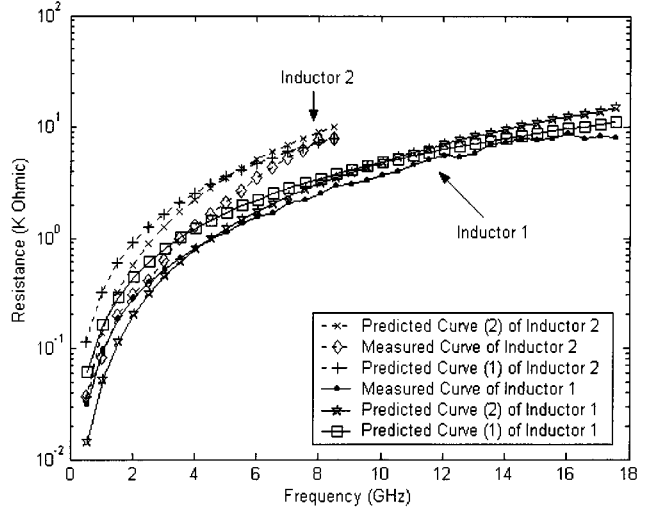
TABLE I
OPTIMIZED VALUES OF CIRCUIT COMPONENTS FOR
SAMPLE INDUCTOR ON GaAs

Circuit Components	Values in Traditional Model	Values in Modified Model
R_s (Ω)	4.741	6.637
R_s' (Ω)		4.617
L_s (H)	2.430×10^{-9}	2.380×10^{-9}
L_s' (H)		581.0×10^{-12}
C_s (F)	19.73×10^{-15}	20.08×10^{-15}
R_{sub1} (Ω)	11.59	11.61
R_{sub2} (Ω)	15.86	15.86
C_{sub1} (F)	37.75×10^{-15}	37.71×10^{-15}
C_{sub2} (F)	28.12×10^{-15}	28.12×10^{-15}

Table I tabulates the Inductor 1 model components' value of Figs. 2 and 3 after optimization. As noted from this table, the value for R_s has changed drastically from 4.741 to 6.637 Ω. The inductor value L_s, as noted, remains relatively constant.

VI. CONCLUSIONS

In this paper, an improved expression incorporating the skin effect for the prediction of the series resistance in a spiral inductor model has been derived. A novel modified equivalent-circuit model based on eddy-current analysis has thus been proposed. Good agreement between the simulated and measured S-parameters have been obtained.

REFERENCES

[1] W. B. Kuhn and N. K. Yanduru, "Spiral inductor substrate loss modeling in silicon RFIC's," *Microwave J.*, pp. 66–81, Mar. 1999.

[2] W. B. Kuhn and N. M. Ibrahim, "Analysis of current crowding effects in multiturn spiral inductors," *IEEE J. Trans. Microwave Theory Tech.*, vol. 49, pp. 31–38, Jan. 2001.

[3] J. R. Long and M. A. Copeland, "The modeling, characterization and design of monolithic inductors for silicon RF IC's," *IEEE J. Solid-State Circuits*, vol. 32, pp. 357–369, Mar. 1997.

[4] C. P. Yue and S. S. Wong, "Physical modeling of spiral inductors on silicon," *IEEE Trans. Electron Devices*, vol. 47, pp. 560–568, Mar. 2000.

[5] A. M. Niknejad and R. G. Meyer, "Analysis, design and optimization of spiral inductors and transformers for Si RF IC's," *IEEE J. Solid-State Circuits*, vol. 33, pp. 1470–1481, Oct. 1998.

[6] R. D. Lutz, Y. Hahm, A. Weisshaar, V. K. Tripathi, A. Grzegorek, and W. McFarland, "Modeling of spiral inductors on lossy substrates for RFIC," in *IEEE MTT-S Int. Microwave Symp. Dig.*, May 1998, pp. 1855–1858.

[7] R. D. Lutz *et al.*, "Modeling of spiral inductors on lossy substrates for RFIC applications," in *Proc. RFIC Symp.*, June 1998, pp. 313–316.

[8] H.-S. Tsai, J. Lin, R. C. Frye, K. L. Tai, M. Y. Lau, D. Kossives, F. Hrycenko, and Y.-K. Chen, "Investigation of current crowding effect on spiral inductors," in *IEEE MTT-S Int. Microwave Symp. Dig.*, 1997, pp. 139–142.

[9] Y. L. Chow and I. N. Behery, "An approximate dynamic spatial Green's function for microstrip lines," *IEEE Trans. Microwave Theory Tech.*, vol. MTT-26, pp. 978–983, Dec. 1978.

Multilayer and Anisotropic Planar Compact PBG Structures for Microstrip Applications

Christophe Caloz and Tatsuo Itoh

Abstract—**Two novel microstrip planar photonic-bandgap (PBG) structures are presented, i.e., a multilayer PBG and an anisotropic PBG. The multilayer PBG, constituted of uniplanar compact (UC) PBGs stacked up below the line, produces huge gaps ($>$140%) through the suppression of parasitic transmission peaks and can achieve a twofold size reduction with respect to UC-PBGs. The anisotropic PBG is a uniplanar structure exhibiting a propagation direction and an attenuation direction (AD) in a working range of the order of 35%, deep/sharp gaps broader than 65% in the AD, an excellent insensitivity to the line position and an extreme compact size of the order of $\lambda/2$ by $\lambda/7$.**

Index Terms—**Anisotropic PBGs, monolayer/multilayer PBGs.**

I. INTRODUCTION

Recently, novel microwave photonic-bandgap (PBG) structures have been proposed [1]. Among those, the uniplanar compact photonic-bandgap (UC-PBG) structure [2], characterized by wide
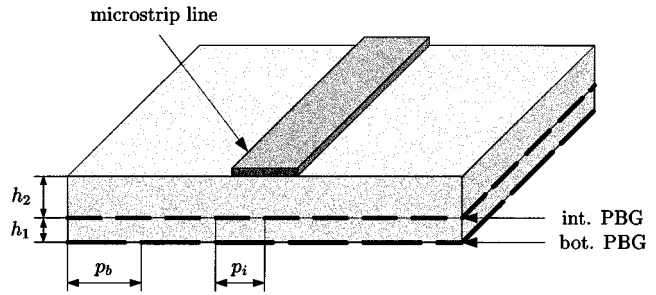
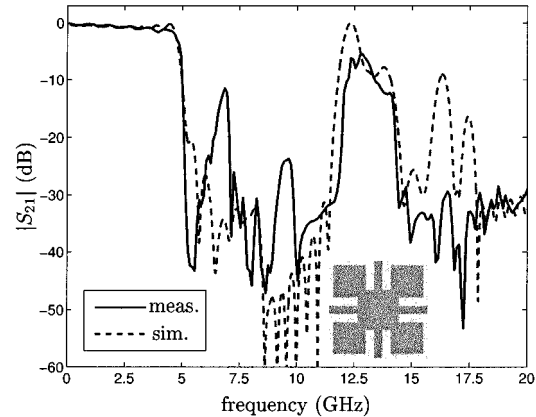Fig. 1.   Multilayer PBG architecture (bilayer case).

Fig. 2.   Insertion loss for the monolayer PBG structure with the unit cell (a) pattern shown in the inset.

stopbands [3] and a slow-wave effect with very low insertion loss [4], is of particular interest because of its easy integration and low cost. Its has been demonstrated in a variety of applications including, for instance, broad-band low-pass and spurious-free bandpass filters [2] and harmonic-tuned power amplifiers [5].

In this paper, we present two novel compact planar microstrip PBG structures, which can be considered as extensions of the UC-PBG, i.e., the multilayer and anisotropic PBGs. The multilayer PBG [6] is an extension of the UC-PBG, in which several UC-PBGs, with different patterns and periods, are stacked up below the microstrip line. This structure provides additional degrees of freedom that are exploited to achieve a dramatic increase in bandwidth and reduction of size. The anisotropic PBG [7] is a uniplanar structure presenting an anisotropic geometry resulting in a propagation direction (PD) and an attenuation direction (AD). This structure also exhibits very good filtering performances in the AD with an extremely compact size.

II. MULTILAYER PBG

The architecture of the multilayer PBG is shown in Fig. 1. We will present two variants of this structure, i.e., a harmonic configuration and an inharmonic configuration. The bottom PBG of the harmonic configuration is the conventional UC-PBG, shown in the inset of Fig. 2, and with a period $p_b = a$. The intermediate PBG (shown in the inset of Fig. 3) has the same pattern, except that the strip branches have been removed and presents a period twice smaller ($p_i = p_b/2 = a/2$). This configuration is called *harmonic* because the periods of the two PBGs are in a harmonic ratio, which results from superimposition into a structure of global period identical to the larger of the periods ($p_g = p_b = a$). Since the cutoff frequency is fixed by the larger period, it is expected to remain unchanged with respect to the case of the monolayer PBG of period a.